



## ISTITUTO NAZIONALE DI RICERCA METROLOGICA Repository Istituzionale

Telescope jitters and phase noise in the LISA interferometer

*Original*

Telescope jitters and phase noise in the LISA interferometer / Sasso, Carlo Paolo; Mana, Giovanni; Mottini, Sergio. - In: OPTICS EXPRESS. - ISSN 1094-4087. - 27:12(2019), p. 16855-16870. [10.1364/OE.27.016855]

*Availability:*

This version is available at: 11696/62221 since: 2020-05-19T14:59:10Z

*Publisher:*

Optical Society of America

*Published*

DOI:10.1364/OE.27.016855

*Terms of use:*

This article is made available under terms and conditions as specified in the corresponding bibliographic description in the repository

*Publisher copyright*

(Article begins on next page)



# Telescope jitters and phase noise in the LISA interferometer

CARLO PAOLO SASSO,<sup>1,\*</sup> GIOVANNI MANA,<sup>1</sup> AND SERGIO MOTTINI<sup>2</sup>

<sup>1</sup>INRIM – Istituto Nazionale di Ricerca Metrologica, Str. delle cacce 91, 10135 Torino, Italy

<sup>2</sup>Thales Alenia Space, Str. antica di Collegno, 253, 10146 Torino, Italy

\*c.sasso@inrim.it

**Abstract:** The Laser Interferometer Space Antenna aims to measure picometer changes of the  $2.5 \times 10^6$  km sides of a triangular constellation of satellites. Each spacecraft hosts two telescopes that simultaneously transmit and receive laser beams measuring the constellation arms by heterodyning the received wavefronts with local references. We report an end-to-end investigation of the measurement noise due to the interaction between the telescope jitters and wavefront aberrations. With provisional design parameters, to achieve the targeted sensitivity the root-mean-square aberrations must be less than  $\lambda/65$ .

© 2019 Optical Society of America under the terms of the [OSA Open Access Publishing Agreement](#)

## 1. Introduction

The Laser Interferometer Space Antenna (LISA) – an equilateral triangle of three spacecraft with a side length of  $2.5 \times 10^6$  km – aims to measure picometer changes in the distance between free-falling masses placed inside the spacecraft [1, 2]. As shown in Fig. 1, the measurement is split into two steps: i) the measurement of the test-mass motions with respect to onboard optical-benches and ii) the measurement of the spacecraft distance. To this end, each satellite is equipped with two telescopes (afocal, off-axis, beam expanders having provisional 134× magnification) that simultaneously transmit and receive 1064 nm laser beams and heterodyne the received beams with local references [3, 4]. A critical aspect is the total displacement noise in a one way test-mass to test-mass link [3],

$$S_{\text{IFO}}^{1/2} = 10 \frac{\text{pm}}{\sqrt{\text{Hz}}} \sqrt{1 + \left( \frac{2 \text{ mHz}}{f} \right)^4}, \quad (1)$$

in the frequency band from 0.1 mHz to 0.1 Hz. This requirement imposes tight constraints on the phase of the received wavefront and the stability of the interfering beams. The shot noise contribution is about  $5 \text{ pm}/\sqrt{\text{Hz}}$ , and the local part of that measurement has been demonstrated in LISA Pathfinder [5].

For the transmission, each telescope takes a collimated beam, with a diameter of 2.24 mm, and transforms it into a beam having a 300 mm diameter. For the reception, each telescope collects, with a 300 mm diameter aperture, the light sent by the far spacecraft and reduces it to a 2.24 mm diameter beam. Each telescope operates between a pair of conjugate pupils and maps angular motions in the sky into angular movements in an optical bench without any transverse displacement, and ideally without length instabilities.

Wavefront aberrations and telescope jitters interact and cause a measurement noise. Firstly, because of aberrations, the received wavefront deviates from sphericity. Therefore, the transmitter jitter leads to changes of received phase and, consequently, to apparent variations of the spacecraft distance [6, 7]. Secondly, the receiver jitter misaligns the interfering beams and leads to additional phase changes of the heterodyne signal [8, 9].

The wavefronts quality, both in the transmission and reception, must be good enough that the expected  $10 \text{ nrad}/\sqrt{\text{Hz}}$  jitters do not cause phase noise in the heterodyne signal [3, 4]. In

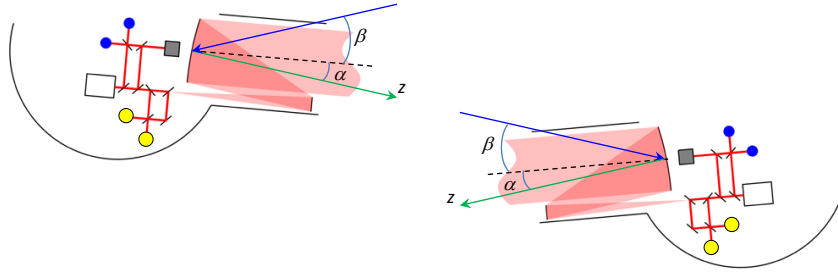


Fig. 1. Schematic of the LISA measurement. The time-of-flight of the light separates the snapshots of the two spacecraft. Each telescope transmits and receives light to and from the other. The transmitted light is phase locked to the received one, setting up a transponder-like scheme. The grey boxes are the test masses; the dots indicate where the test-mass motion (blue) and spacecraft distance (yellow) are measured. The dashed lines are the axes of the transmitted beams. The green arrows are the  $z$  axes; the blue arrows are the line-of-sight to the far spacecrafts;  $\alpha$  and  $\beta$  are the transmission and reception angles; we assume that the local beam is parallel to the transmitted one. Adapted from [2]

previous papers, we investigated separately the noise originating from the transmitter and receiver jitter [10, 11].

In this paper, we build on those results and report about an end-to-end study of the measurement noise from the beam launch to the far field and from the reception to the heterodyne signal. Since the relationship between the measured and actual distances is computationally expensive, we used an analytic parametric surrogate for the phase of the heterodyne signal and its sensitivity to jitter. It takes the form of a polynomial expansion and allows for fast sampling from the possible wavefront aberrations. When studying the phase sensitivity to the jitter, it is possible to single out the root-mean-square deviation from flatness of the wavefronts as a global parameter predicting the mean noise.

Sections 2 and 3 model the far-field propagation of the transmitted wavefront and interference. Sections 4.2 and 4.3 give the polynomial approximations of the far-field and heterodyne-signal phases, which are the main results of our previous studies. Section 4.4 works on these approximations and provides the noise and sensitivity to the jitters of the heterodyne signal. In section 5 we carry out a Monte Carlo simulation of the measurement noise by sampling from random wavefront aberrations, examine how the sensitivity to the jitters depends on the design parameters and aberrations, and develop criteria for the noise assessment.

## 2. Far-field propagation

By using the scalar and paraxial approximations, the optical field propagating between the spacecraft is

$$E(\mathbf{r}, z; t) = u(\mathbf{r}; z)e^{-i(kz - \omega t)}, \quad (2)$$

where  $z$  is the propagation distance,  $\mathbf{r} = \{x, y\}$  is a position vector in a plane transverse to the  $z$  axis,  $\omega$  is the angular frequency,  $k = \omega/c = 2\pi/\lambda$  is the wave number,  $\lambda = 1064$  nm is the wavelength. Owing to the finite speed of light and the relative spacecraft motion, the  $z$  axis points the receiving telescope at about 16 s forward the observation direction (see Fig. 1).

The complex amplitude of the transmitted beam,

$$u(\mathbf{r}; 0) = e^{-r^2/w_{TX}^2} e^{-iS_{TX}(\mathbf{r})}, \quad (3)$$

is assumed to have a Gaussian intensity-profile, where  $w_{TX}$  is the  $1/e^2$  beam-radius and  $S_{TX}(\mathbf{r})$  is a small and zero-mean wavefront aberration.

The paraxial propagation in free space is given by the Rayleigh-Sommerfeld integral

$$u(\mathbf{r}; z) = \frac{ik e^{-ikr^2/(2z)}}{2\pi z} \int_{\mathcal{M}} e^{ik\mathbf{r} \cdot \boldsymbol{\xi}/z} e^{-\xi^2/w_{TX}^2} e^{-iS_{TX}(\boldsymbol{\xi})} d\boldsymbol{\xi}, \quad (4)$$

where  $\boldsymbol{\xi}$  is a dummy position vector in the  $z = 0$  input plane,  $\mathcal{M}$  is the area of the primary mirror – a disk having  $r_{TX} \approx 150$  mm radius – and the  $\exp[ik\xi^2/(2z)]$  kernel factor has been included in  $\exp[-iS_{TX}(\boldsymbol{\xi})]$  as an additional defocus.

We approximate the received field by the spherical wave

$$u(\mathbf{r}; z) \approx \frac{ik |u(0; z)| e^{-i[kr^2/(2z) + \phi_{far}]}{2\pi z} \quad (5)$$

where  $\phi_{far} = \arg[u(0; z)]$  is the advance or delay with respect to the dynamical phase  $kz$ ,

$$u(0; z) = \int_{\mathcal{M}} e^{-\xi^2/w_{TX}^2} e^{iS_{TX}(\boldsymbol{\xi})} d\boldsymbol{\xi} = \int_0^{r_{TX}} \xi e^{-\xi^2/w_{TX}^2} \left( \int_0^{2\pi} e^{-iS_{TX}(\boldsymbol{\xi})} d\theta \right) dr \quad (6)$$

is the on-axis amplitude of the far field, and  $r$  and  $\theta$  are the radial and azimuthal coordinates.

### 3. Heterodyne interferometry

We describe the local,

$$E_1(\mathbf{r}; t) = u_1(\mathbf{r}), \quad (7)$$

and received,

$$E_2(\mathbf{r}; t) = u_2(\mathbf{r}) e^{-i(kz + \phi_{far} + \Omega t)}, \quad (8)$$

optical fields on the detector plane by the complex amplitudes

$$u_1(\mathbf{r}) = e^{-r^2/w_1^2} e^{-iS_1(\mathbf{r})}, \quad (9)$$

and

$$u_2(\mathbf{r}) = e^{-r^2/w_2^2} e^{-iS_2(\mathbf{r})}, \quad (10)$$

where we omitted the common term  $e^{i\omega t}$ ,  $z$  is the spacecraft distance,  $\phi_{far}$  is the far-field phase of the transmitted wavefront,  $S_1(\mathbf{r})$  and  $S_2(\mathbf{r})$  are small, zero mean, deviations from flat wavefronts,  $\mathbf{r} = (x, y)^T$  is a position vector in the detector plane,  $w_1$  and  $w_2$  are the beam radii, and  $\Omega$  is the heterodyne angular frequency.

In (5), due to the negligible size of the telescope aperture relative to the size of the received beam, we approximated the received wavefront by a spherical one having a phase delay (or advance)  $\phi_{far}$  that depends on the transmission angle and aberrations. The propagation through the receiver optics introduce anew wavefront aberrations, which are summarized by  $S_2(\mathbf{r})$ .

Though they matter in terms of contrast and shot noise, the interfering-beam amplitudes do not affect the phase of the interference signal. Therefore, we set both to unity. By neglecting the piston terms of  $S_1(\mathbf{r})$  and  $S_2(\mathbf{r})$ , we do not consider the phase retardation related to the optical lengths of the beam paths through the receiving telescope and optical bench.

The phase of the heterodyne signal is  $kz + \phi$ , where

$$\phi = \phi_{far} + \phi_{\Xi} \quad (11)$$

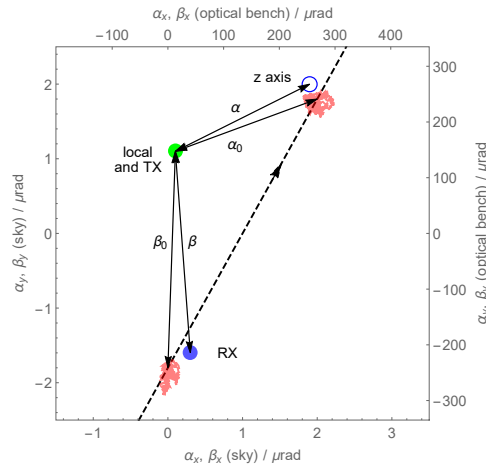


Fig. 2. Hypothetical angular map of the beams (green: local and transmitted, blue: received) contributing to the measurement of the spacecraft distance. The two scales, one magnified 134 times, provide the angles in the sky and optical bench. For the sake of simplicity, we assumed the local and transmitted beams parallel. The far spacecraft moves along the dashed line; the circle is the  $z$  axis (the far spacecraft after a light round trip). The telescope jitter makes the line-of-sight to the far spacecraft and the  $z$  axis noisy (red random walks);  $\alpha$  and  $\beta$  are the (instantaneous) transmission and reception angles;  $\alpha_0$  and  $\beta_0$  are their mean values.

is the phase advance (or delay) to the dynamical one,  $\phi_{\Xi} = \arg(\Xi)$ , and

$$\Xi = \int_{\mathcal{D}} u_1^*(\mathbf{r}) u_2(\mathbf{r}) d\mathbf{r} = \int_0^{r_D} r e^{-2r^2/w_{RX}^2} \left( \int_0^{2\pi} e^{-iS_{RX}(\mathbf{r})} d\theta \right) dr \quad (12)$$

is the interference signal. In (12),  $\mathcal{D}$  is the detector area (a disk having  $r_D \approx 1.1$  mm radius),  $w_{RX}^2 = 2w_1^2 w_2^2 / (w_1^2 + w_2^2)$  is the harmonic mean of  $w_1^2$  and  $w_2^2$ ,  $S_{RX}(\mathbf{r}) = S_2(\mathbf{r}) - S_1(\mathbf{r})$  is a small deviation from flatness of the interference-pattern phase, and  $r$  and  $\theta$  are the radial and azimuthal coordinates.

The  $\phi_{far}$  phase depends on the transmission angle  $\alpha$  through the tilt component of  $S_{TX}$ . The transmission is on-axis and  $\alpha$  is null when the tilt aberration of  $S_{TX}$  is zero and the transmitted beam propagates along the  $z$  axis (see Figs. 1 and 2). The  $\phi_{\Xi}$  phase depends on the reception angle  $\beta$  through the tilt component of  $S_{RX}$ . The reception is on-axis and  $\beta$  is null when the tilt aberration of  $S_{RX}$  is zero and the received and local beams propagate in parallel (see Figs. 1 and 2).

In (10), we assumed a Gaussian intensity profile. However, if the receiver is modelled as an ideal beam-expander, the interference is between a local Gaussian beam and a received top-hat beam. Both Gaussian and (ideal) top-hat beams are limit cases. Furthermore,  $\phi_{far}$  and  $\phi_{\Xi}$  require the evaluation of the same integrals (6) and (12). In the Gaussian beam limit case here considered, they differ only by the replacement of  $w_{RX}^2$  with  $2w_{TX}^2$ . In the top-hat limit case, they are identical.

## 4. Phase noise

### 4.1. Zernike modes

The phase profiles  $S_{TX}(\mathbf{r})$  and  $S_{RX}(\mathbf{r})$  are expressed in terms of Zernike modes. Therefore,

$$S_{TX,RX}(\mathbf{r}) = \sum_{n=1}^{\infty} \sum_{m=-n}^n z_n^m R_n^{|m|}(\rho) e^{im\theta} = \sum_{n=1}^{\infty} \sum_{m=-n}^n z_n^m Z_n^m(\rho, \theta), \quad (13)$$

where the radial polynomial are null for all  $n - |m|$  odd or negative,  $\rho = |\mathbf{r}|/r_{\text{TX},D}$  is the normalized radial coordinate, and  $\theta$  is the azimuth. The Zernike polynomials  $Z_n^m(\rho, \theta)$  satisfy the orthogonality relation

$$\int_0^{2\pi} \int_0^1 Z_n^m(\rho) Z_{n'}^{m'}(\rho) \rho d\rho d\theta = \frac{\pi \delta_{n,n'} \delta_{m,m'}}{n+1}. \quad (14)$$

To ensure that  $S_{\text{TX,RX}}(\mathbf{r})$  are real, the relationship  $z_n^{-m} = z_n^{m*}$  holds. Therefore,  $z_n^0$  are real and, if  $m \neq 0$ ,  $z_n^{\pm m} = |z_n^m| e^{\pm i\theta_n^m}$ , where  $|z_n^{-m}| = |z_n^m|$ . Eventually, the magnitudes  $|z_n^m|$  are expressed in radians. The  $n = 1$  term,

$$\begin{aligned} z_1^{-1} \rho e^{-i\theta} + z_1^1 \rho e^{i\theta} &= 2|z_1^1| \rho \cos(\theta + \theta_1^1) \\ &= \begin{cases} kr_{\text{TX}} \alpha \rho \cos(\theta + \theta_1^1) & \text{transmitted wavefront} \\ kr_{\text{RX}} \beta \rho \cos(\theta + \theta_1^1) & \text{detected wavefronts} \end{cases}, \end{aligned} \quad (15)$$

where  $r_{\text{RX}} = Mr_D$  and  $z_1^1 = |z_1^1| e^{i\theta_1^1}$  takes the transmission,

$$\alpha = 2|z_1^1|/(kr_{\text{TX}}), \quad (16)$$

and reception,

$$\beta = 2|z_1^1|/(kr_{\text{RX}}), \quad (17)$$

angles into account.

We will also use the in-plane and out-of-plane components  $\zeta_x = |z_1^1| \cos(\theta_1^1)$ ,  $\zeta_y = |z_1^1| \sin(\theta_1^1)$ ,  $\alpha_x = \alpha \cos(\theta_1^1)$ ,  $\alpha_y = -\alpha \sin(\theta_1^1)$ . Similar equations hold for the  $\eta_{x,y}$  and  $\beta_{x,y}$  components of the reception angle.

#### 4.2. Far-field phase.

By expressing  $S_{\text{TX}}(\mathbf{r})$  in term of Zernike modes and limiting the analysis to the lowest order couplings between tilt and higher-order aberrations, the phase of the received wavefront in advance or delay to the  $kz$  retardation is

$$\phi_{\text{far}} = \arg[u(0; z)] \approx a_{00} + a_{10}\zeta_x + a_{20}\zeta_x^2 + a_{01}\zeta_y + a_{02}\zeta_y^2 + a_{11}\zeta_x\zeta_y, \quad (18)$$

where  $u(0; z)$  is given by (6),

$$\zeta_x = kr_{\text{TX}}\alpha_x/2, \quad (19)$$

$$\zeta_y = kr_{\text{TX}}\alpha_y/2, \quad (20)$$

are the directional components of the  $z_1^1$  tilt aberration of the transmitted wavefront with respect to a flat one orthogonal to the  $z$  axis,  $\alpha_x$  and  $\alpha_y$  are the directional components of the transmission angle, and  $r_{\text{TX}}$  is the radius of the primary mirror. A null angle, i.e.,  $\alpha = 0$ , means that the transmission occurs along the  $z$  axis.

The  $a_{ij}$  coefficients – which we derived in [10] – depend on the normalized radius of the transmitted beam,  $w'_{\text{TX}} = w_{\text{TX}}/r_{\text{TX}}$ , and the modal amplitudes  $z_n^m$  of the transmitted wavefront. By limiting the aberrations to defocus, astigmatism, coma, trefoil, and spherical, they are given in the appendix.

As shown in [7, 10], for each specific wavefront aberration  $S_{\text{TX}}$ , there exists an optimal transmission angle  $\alpha_{\text{opt}}$  – which can be found by solving  $\nabla_{\alpha} \phi_{\text{far}} = 0$  – that nullifies the  $\phi_{\text{far}}$  sensitivity to the transmission angle.

### 4.3. Heterodyne-signal phase.

To study the phase of the heterodyne signal, we express the misalignment of the interfering beams in term of the reception angle  $\beta$ , where  $\beta = 0$  rad means that the interfering beams are parallel. Therefore, the angle  $\beta$  means that the tilt aberration  $z_1^1$  of the phase profile  $S_{RX}(\mathbf{r})$  is associated with the  $M\beta$  misalignment of the interfering beams, where  $M \approx 134$  is the telescope magnification.

By expressing the phase profile  $S_{RX}(\mathbf{r})$  in terms of Zernike modes and limiting the analysis to the lowest order couplings between tilt and higher-order aberrations, we obtain

$$\phi_{\Xi} = \arg(\Xi) \approx b_{00} + b_{10}\eta_x + b_{20}\eta_x^2 + b_{01}\eta_y + b_{02}\eta_y^2 + b_{11}\eta_x\eta_y, \quad (21)$$

where  $\Xi$  is given by (12),

$$\eta_x = kr_{RX}\beta_x/2, \quad (22)$$

$$\eta_y = kr_{RX}\beta_y/2, \quad (23)$$

are the directional components of the  $z_1^1$  (differential) tilt aberration of the interfering wavefronts,  $\beta_x$  and  $\beta_y$  are the directional components of the reception angle,  $r_{RX} = Mr_D$  is the effective detector radius, and  $r_D$  is the detector radius.

The  $b_{ij}$  coefficients – which we derived in [11] – depend on the normalized mean-radius of the interfering beams  $w'_{RX} = w_{RX}/r_D$  and the amplitudes of the phase-profile aberrations. By limiting the aberrations to defocus, astigmatism, coma, trefoil, and spherical, they are given in the appendix. Owing to the identity of the (6) and (12) integrals, the  $a_{ij}$  and  $b_{ij}$  coefficients in (18) and (21) are linked by  $a_{ij}(w') = b_{ij}(\sqrt{2}w')$ .

As shown in [11], for each specific aberration  $S_{TX}$  of the interference phase-profile there exists an optimal reception angle  $\beta_{opt}$  – which can be found by solving  $\nabla_{\beta}\phi_{\Xi} = 0$  – that nullifies the  $\phi_{\Xi}$  sensitivity to the reception angle.

### 4.4. Phase noise.

To compensate for the disturbances, the telescope pointings are continuously corrected, which corrections jitter both the transmission and reception angles and, according to (18) and (21), interfere with the phase of the heterodyne signal (see Fig. 2). The LISA error budgeting is done in the frequency domain, with noises expressed as power spectral densities. However, since no dynamics is involved in the propagation of the wavefronts, the transfer function that maps jitters into phase noise is independent of frequency. Therefore, we considered white uncorrelated jitters and computed how the jitter variance propagates into the phase-noise variance.

By linearization of (18) and (21), the variance of the  $\phi = \phi_{far} + \phi_{\Xi}$  phase is

$$\sigma_{\phi}^2 \approx [|\nabla_{\alpha}\phi_{far}|_0^2 + |\nabla_{\beta}\phi_{\Xi}|_0^2]\sigma_{jitter}^2/4, \quad (24)$$

where  $\sigma_{jitter}^2$  is the variance of the jitter magnitude and  $\nabla_{\alpha,\beta}$  are gradients over  $\alpha$  and  $\beta$  [12]. The 1/4 factor originates from the relationship between the Rayleigh distribution of the jitter magnitude and that of its directional components.

The transfer function is  $\mathfrak{H} = \sigma_{\phi}/\sigma_{jitter}$ , where

$$\begin{aligned} \mathfrak{H}^2 &\approx \frac{1}{4} [|\nabla_{\alpha}\phi_{far}|_0^2 + |\nabla_{\beta}\phi_{\Xi}|_0^2] \\ &= \left(\frac{kw_{TX}}{4}\right)^2 [(a_{10} + 2a_{20}\zeta_{0x} + a_{11}\zeta_{0y})^2 w_{TX}'^{-2} + (a_{01} + 2a_{02}\zeta_{0y} + a_{11}\zeta_{0x})^2 w_{TX}'^{-2} \\ &\quad + (b_{10} + 2b_{20}\eta_{0x} + b_{11}\eta_{0y})^2 w_{RX}'^{-2} + (b_{01} + 2b_{02}\eta_{0y} + b_{11}\eta_{0x})^2 w_{RX}'^{-2}], \end{aligned} \quad (25)$$



the 0x and 0y subscripts label the mean values of  $\zeta_{x,y}$  and  $\eta_{x,y}$ , and we used (19), (20), (22), and (23). Furthermore, we parameterize the result by  $w'_{TX} = w_{TX}/r_{TX}$  and  $w'_{RX} = w_{RX}/r_D = w_{TX}/r_{RX}$ , and used  $w_{TX} = Mw_{RX}$ .

The  $a_{ij}$  and  $b_{ij}$  coefficients depend on the amplitudes of the Zernike modes. To find a criterion for the noise assessment, we need an expression determined by the deviations of the wavefront from flatness alone. The sought expression can be obtained by averaging  $\xi^2$  over the  $z_n^m$  amplitudes constrained to a predetermined root-mean-square amplitude  $\sigma_S$  of the wavefront aberrations. Therefore, the amplitudes of the Zernike modes of  $S_{TX}$  and  $S_{RX}$  are constrained by

$$\sum_{n=2}^{\infty} \sum_{m=0}^n \frac{c_n^m |z_n^m|^2}{n+1} = \sigma_S^2, \quad (26)$$

where  $c_n^m = 1$  if  $m = 0$  and  $c_n^m = 2$  otherwise. In the following, we set  $\sigma_S = 74$  mrad. The average peak-to-valley deviation from flatness of a wavefront having this root-mean-square aberration-amplitude is about  $\lambda/16$ , with a 15% standard deviation.

By averaging over the azimuths  $\theta_n^m$  of the  $z_n^m$  amplitudes – which are assumed identical, independent, and uniformly distributed – we average over all the orientations of the Zernike modes. Since the  $\theta_n^m$  origin is arbitrary, we can set the tilt azimuth to zero, so that the average,  $\langle \xi^2 \rangle_{\theta_n^m}$ , cannot depend on the directional tilt-components. Hence, we obtain

$$\langle \xi^2 \rangle_{\theta_n^m} \approx g_0(w'_{TX}) + g_0(w'_{RX}) + g_2(w'_{TX})\alpha_0^2 + g_2(w'_{RX})\beta_0^2, \quad (27)$$

where

$$\begin{aligned} \sqrt{\eta_{0x}^2 + \eta_{0y}^2} &= kr_{RX}\beta_0/2 = kw_{TX}\beta_0/(2w'_{RX}), \\ \sqrt{\zeta_{0x}^2 + \zeta_{0y}^2} &= kr_{TX}\alpha_0/2 = kw_{TX}\alpha_0/(2w'_{TX}), \end{aligned} \quad (28)$$

and  $\alpha_0 = (\alpha_{0x}^2 + \alpha_{0y}^2)^{1/2}$  and  $\beta_0 = (\beta_{0x}^2 + \beta_{0y}^2)^{1/2}$  are the mean values of the transmission and reception angles (see Fig. 2). The polynomial coefficients were calculated analytically with the aid of Mathematica [13] by limiting the aberrations to defocus, astigmatism, coma, trefoil, and spherical. The results are

$$g_0(w') = \left( \frac{kw_{TX}}{4w'} \right)^2 \left[ (Dz_2^0 + Gz_4^0)^2 |z_3^1|^2 + (C^2 |z_3^1|^2 + B^2 |z_3^3|^2) |z_2^2|^2 \right], \quad (29)$$

$$g_2(w') = \left( \frac{kw_{TX}}{2w'} \right)^4 \left[ F^2 |z_2^2|^2 + (Ez_2^0 + Hz_4^0)^2 \right], \quad (30)$$

where  $B, C, D, E, F, G$ , and  $H$  depend on the normalized radius  $w'$  as given in (42-50).

The average over the magnitude  $|z_n^m|$  of the Zernike modes requires to integrate the polynomials (29) and (30) over the hyperellipsoid (26). A derivation of these integrals is in [14]. The result is

$$\langle \xi^2 \rangle_{z_n^m} \approx [\overline{g_0(w'_{TX})} + \overline{g_0(w'_{RX})}] \sigma_S^4 + \overline{g_2(w'_{TX})} \sigma_S^2 \alpha_0^2 + \overline{g_2(w'_{RX})} \sigma_S^2 \beta_0^2, \quad (31)$$

where

$$\overline{g_0(w')} = \left( \frac{kw_{TX}}{4w'} \right)^2 \frac{1}{35} (3B^2 + 3C^2 + 6D^2 + 10G^2), \quad (32)$$

$$\overline{g_2(w')} = \left( \frac{kw_{TX}}{2w'} \right)^4 \frac{1}{10} (6E^2 + 3F^2 + 10H^2). \quad (33)$$



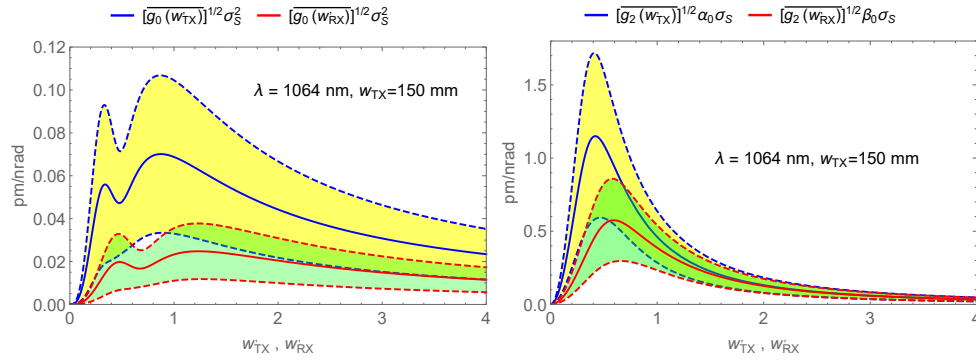


Fig. 3. On-axis (left) and off-axis (right, the angles  $\alpha_0$  and  $\beta_0$  are set to 1  $\mu$ rad) sections of  $\langle \xi^2 \rangle_{z_n^m}$  vs. the normalized radii of the transmitted and detected beams,  $w'_{TX}$  and  $w'_{RX}$ . The filled areas indicate the standard-deviations. Blue: transmission; red: reception. The root-mean-square amplitude of  $S_{TX}$  and  $S_{RX}$  is 74 mrad.

According to (31),  $\alpha_0 = \beta_0 = 0$  rad minimize, on the average, the phase noise. Therefore, after averaging over the possible transmitter and receiver aberrations, to minimize the contributions of the jitters to the phase noise, both the transmission and reception must be on-axis. In the case of off-axis arrangements, the quadratic terms of (31) prevail. In fact, they are of the order of  $\sigma_S^2$ , while the constant ones are of the order of  $\sigma_S^4$ .

## 5. Results

The jitter and aberrations of the transmitter and receiver contribute to the noise of the interferometric measurement. The received wavefront was approximated by a plane one whose phase  $\phi_{far}$  advances or delays with respect the dynamical one (encoding the sought distance) because of the transmitter jitter and aberrations. An ideal receiver – that is, a perfect compressor – does not aberrate the received wavefront, also if we take the truncation into account. The additional advance or delay  $\phi_{\Xi}$  of the signal phase takes the receiver non-ideality and jitter into account. Eventually, the average of the transfer function (25) over aberrations having the same root-mean-square amplitude summarizes the noise contributions of both the transmitter and receiver.

The asymptotic values,

$$\langle \xi^2 \rangle_{z_n^m}^{1/2} \approx \begin{cases} \left[ \overline{g_0(w'_{TX})} + \overline{g_0(w'_{RX})} \right]^{1/2} \sigma_S^2 & \text{if } \alpha_0 \approx \beta_0 \approx 0 \text{ rad} \\ \left[ \overline{g_2(w'_{TX})} \right]^{1/2} \sigma_S \alpha_0 & \text{if } \beta_0 = 0 \text{ rad, } kw_{TX}\alpha_0/2 \gtrsim 0.5 \text{ rad} \\ \left[ \overline{g_2(w'_{RX})} \right]^{1/2} \sigma_S \beta_0 & \text{if } \alpha_0 = 0 \text{ rad, } kw_{TX}\beta_0/2 \gtrsim 0.5 \text{ rad} \end{cases} \quad (34)$$

are shown in Fig. 3. To quantify the dispersion of the  $\xi^2$  values, we calculated the standard deviations of  $10^4$   $g_0(w')$  and  $g_2(w')$  values when the angles  $\alpha_0$  and  $\beta_0$  are 1  $\mu$ rad and the root-mean-square amplitudes of  $S_{TX}$  and  $S_{RX}$  is  $\sigma_S = 74$  mrad. In practice, the azimuths  $\theta_2^0$ ,  $\theta_3^1$ , and  $\theta_3^3$  were drawn independently and uniformly in the  $[-\pi, +\pi]$  interval. Those of  $z_2^0$  and  $z_4^0$  were chosen with equal probability zero or  $\pi$ . Eventually, the magnitudes  $|z_2^0|$ ,  $|z_2^2|$ ,  $|z_3^1|$ ,  $|z_3^3|$ , and  $|z_4^0|$  were generated as independent normal variables and then projected onto the hyperellipsoid (26) [15, 16]. This same procedure was used for the subsequent Monte Carlo calculations.

As shown in Fig. 3, when the normalized radii of the transmitted and detected beams,  $w'_{TX} = w_{TX}/r_{TX}$  and  $w'_{RX} = w_{RX}/r_D$  tend to zero (non-truncated Gaussian-beam approximation)

and infinity (plane-wave approximation) the heterodyne signal is insensitive to the jitter. Also, as shown in Fig. 3 (left), the on-axis terms  $\overline{g_0(w'_{TX})\sigma_S^4}$  and  $\overline{g_0(w'_{RX})\sigma_S^4}$  of (31) do not contribute to  $\langle \xi^2 \rangle_{z_n^m}$ . Figure 3 (right) shows that the off-axis terms are maximum when the normalized radii are  $w'_{TX} \approx 0.4$  and  $w'_{RX} \approx 0.6$ , with  $\overline{g_2(w'_{TX})\sigma_S^2}$  (blue line) predominates over  $\overline{g_2(w'_{RX})\sigma_S^2}$  (red line).

The parabolic approximations (18) and (21) hold if  $S_{TX,RX} < 1$  rad over the effective domains of the integrations (4) and (12). However, while the wavefront deviations from flatness satisfy this constraint for all practical purposes, we would like (18) and (21) to be satisfactory approximations for tilt aberrations as significant as possible. Heuristically,  $S_{TX,RX} < 1$  rad implies  $2|z_1^1|w'_{TX,RX} < 1$  rad or, equivalently,  $\alpha < 1/(kw_{TX})$  and  $\beta < 1/(kMw_{RX}) = 1/(kw_{TX})$ . By using  $w_{TX} = 150$  cm, we obtain  $\alpha, \beta \lesssim 1 \mu\text{rad}$ .

To test the accuracy of the approximations made, Fig. 4 compares (18) against the numerical integration of (6). Since (6) cannot depend on the azimuth origin, we can always set  $\theta_1^1 = 0$  and express it in term of the transmission angle  $\alpha$ . The approximation is good up to about  $1 \mu\text{rad}$  and acceptable up to about  $3 \mu\text{rad}$ . It is worth noting that – since the square coefficients are of the first order, while those of the linear terms are of the second –  $\phi_{\text{far}}$  and  $\phi_{\Xi}$  are minimum or maximum near to the on-axis transmission/reception.

To quantify the approximation error, we calculated the fractional errors of  $10^4$  approximated  $\phi_{\text{far}}$  values when  $\alpha_0 = 2 \mu\text{rad}$  and the Zernike spectra of  $S_{TX}$  were randomly generated, but constrained to a root-mean-square amplitude  $\sigma_S = 74$  mrad. Figure 4 shows that, on the average, (18) underestimates  $\phi_{\text{far}}$  by about 8%, with a standard deviation of 10%. Since it implies the same integration, the same is true for (21).

As regards the approximation (25) of  $\xi^2$ , since the calculations of  $\nabla_{\alpha}\phi_{\text{far}}$  and  $\nabla_{\beta}\phi_{\Xi}$  are the same, but the width parameter of  $\nabla_{\beta}\phi_{\Xi}$  is scaled down by  $\sqrt{2}$ , the leading  $\xi^2$  term is  $\nabla_{\alpha}\phi_{\text{far}}$  (see Fig. 3, red lines vs. blue lines, and Fig. 11,  $w'_{RX}$  axis vs.  $w'_{TX}$  axis). Also in this case, the Zernike spectra of  $S_{TX}$  were randomly generated, but constrained to a root-mean-square amplitude  $\sigma_S = 74$  mrad. Figure 5 compares the values of  $\nabla_{\alpha}\phi_{\text{far}}$  obtained from (18) against the differentiation of the numerical integration of (6). The figure shows that, when considering large transmission angles, (18) and (21) neglect significant higher-order contributions. Figure 6 shows the histogram of  $10^4$  calculations of the leading  $\partial_{\alpha}\phi_{\text{far}}$  term, where  $\partial_{\alpha}$  is the directional derivative along  $\alpha$  and  $\alpha_0 = 2 \mu\text{rad}$ . Hence, on the average, (25) underestimates  $\xi$  by about 30%, with a standard deviation of 13%.

In the  $\alpha\beta$  plane, the contour lines of  $\langle \xi^2 \rangle_{z_n^m}^{1/2}$  are ellipses having the axes parallel to constant transmission and reception angles. Figure 7 shows the sections  $\beta_0 = 0$  rad and  $\alpha_0 = 0$  rad for varying values of the normalized radius of the transmitted and detected beams. If the normalized radius is null (Gaussian beam approximation), the heterodyne signal is insensitive to jitter. As the normalized radii grow,  $\langle \xi^2 \rangle_{z_n^m}^{1/2}$  increases but returns to zero when the normalized radius tend to infinity (plane waves approximation). When  $w'_{TX} = w'_{RX} = 1$ , Fig. 7 also shows upper and lower bounds calculated as plus/minus one approximate standard deviation

$$\sigma_{\xi} \approx \frac{\sigma_{\xi^2}}{2\langle \xi^2 \rangle_{z_n^m}^{1/2}}, \quad (35)$$

where  $\sigma_{\xi^2}$  was obtained from  $10^4$  Monte Carlo calculations of (25).

To trade off between the jitter, wavefront quality, and transmission/reception angles, Fig. 8 shows the mean jitter transfer function for varying root-mean-square deviations from flatness of the wavefronts. It also proves the agreement between the analytical and Monte Carlo averaging of  $\xi^2$ . The top axis ticks give the mean peak-to-valley deviation from flatness of each Monte Carlo set.

With about  $2 \mu\text{rad}$  beam divergence and a conservative analysis of the achievable optical and

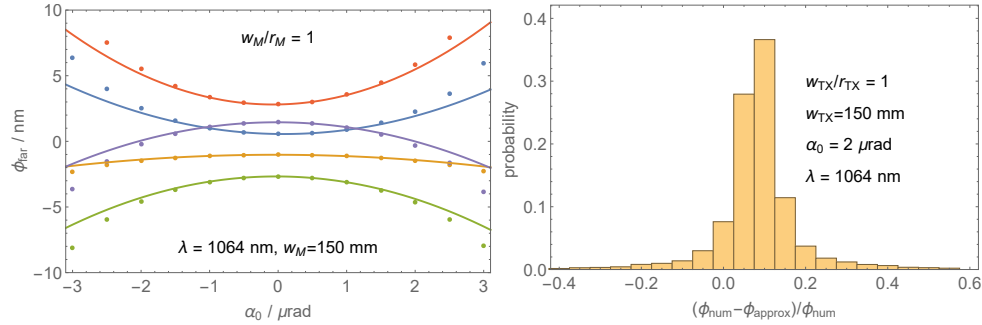


Fig. 4. Left: comparison of the numerical (dots) and approximate (lines) calculations of the far-field phase;  $\alpha_0$  is the transmission angle. Right: histogram of  $10^4$  calculations of the fractional errors when  $\alpha_0 = 2 \mu\text{rad}$ . The Zernike spectra were randomly generated, but constrained to a root-mean-square amplitude of 74 mrad. Colors indicate different runs.

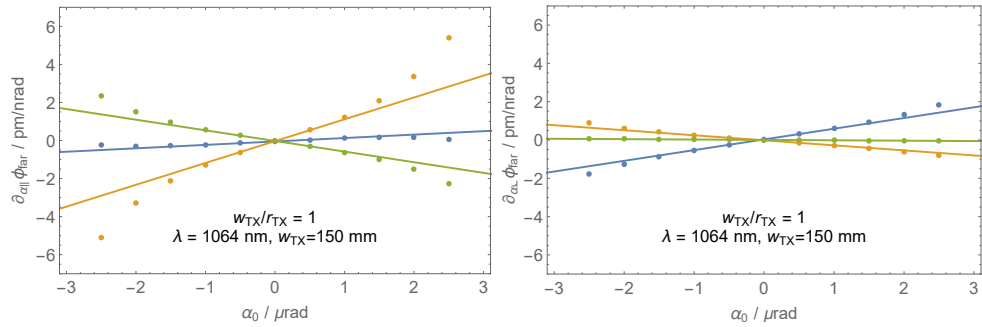


Fig. 5. Comparison of the numerical (dots) and approximate (lines) calculations of  $\nabla_{\alpha} \phi_{\text{far}}$ . Left: the derivative is parallel to  $\alpha_0$ . Right: the derivative is orthogonal to  $\alpha_0$ . The Zernike spectra were randomly generated, but constrained by a root-mean-square amplitude of 74 mrad. Colors indicate different runs

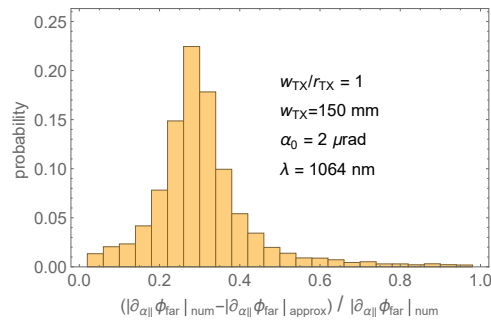


Fig. 6. Histogram of  $10^4$  calculations of the fractional errors of the  $|\partial_{\alpha} \phi_{\text{far}}|$  approximation when  $\alpha_0 = 2 \mu\text{rad}$ . The Zernike spectra were randomly generated, but constrained to a root-mean-square amplitude of 74 mrad.

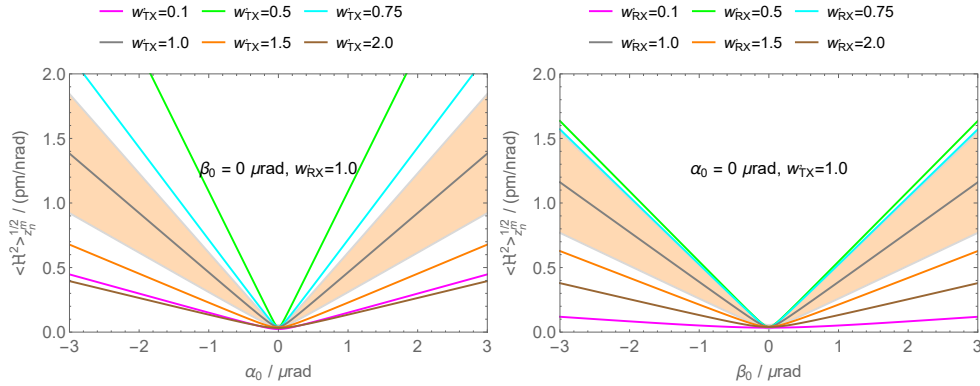


Fig. 7. Sections  $\beta_0 = 0$  rad and  $\alpha_0 = 0$  rad of  $\langle \xi^2 \rangle_{z_n}^{1/2}$  for varying values of the normalized radii  $w'_{TX}$  and  $w'_{RX}$ . In the  $w'_{TX} = w'_{RX} = 1$  case, the bounds (standard deviations) of the  $\xi$ 's values are also given (filled areas). The root-mean-square amplitude of  $S_{TX}$  and  $S_{RX}$  is  $\sigma_S = 74$  mrad. The radius of the transmitted beam is  $w_{TX} = 150$  mm.

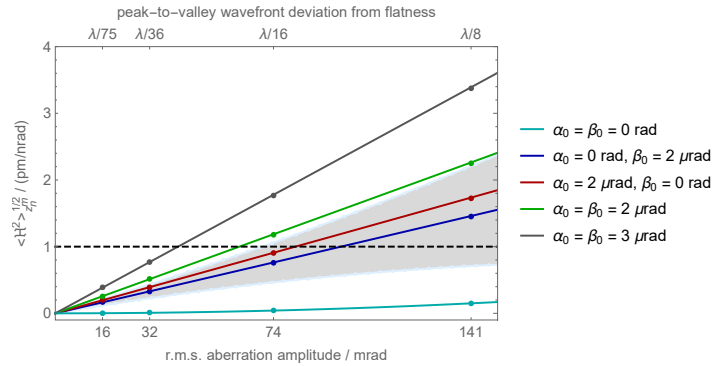


Fig. 8. Mean jitter transfer function for different deviations from flatness of the transmitted and received wavefronts. Dots: numerical (Monte Carlo) average. Solid lines: analytical calculation (31). The top axis ticks are the mean peak-to-valley deviations from flatness of the wavefronts. In the  $\alpha_0 = 0$  mrad and  $\beta_0 = 2$  mrad case, the gray area indicates the bounds (standard deviations) of the Monte Carlo set of  $\xi$ 's values. The normalized radii of the transmitted and detected beams are  $w_{TX}/r_{TX} = w_{RX}/r_D = 1$ . The radius of the transmitted beam is  $w_{TX} = 150$  mm. The horizontal (dashed) line is the upper bound to  $\langle \xi^2 \rangle_{z_n}^{1/2}$  when the design parameters in [3, 4] are taken into account.

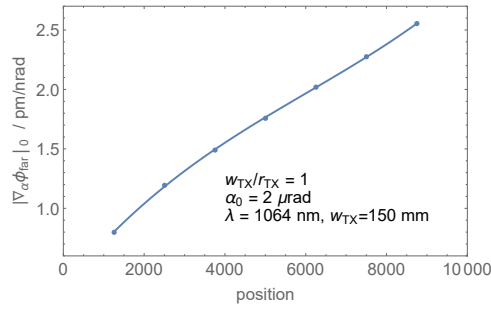


Fig. 9. Moving average (2500 element windows, shifted by 1250 elements) of  $10^4$  sensitivities (sorted in ascending order) of the heterodyne phase to the transmitter jitter. The random wavefront aberrations are constrained by  $\sigma_S = 74$  mrad.

alignment imperfections, to maximise the received power, the transmitter must point the receiver to within 10 nrad [3]. Hence, the transmission angle  $\alpha_0$  is negligible. As regards the reception angle, owing to the point-ahead angle, it cannot be null, unless the local reference is tilted with respect to the transmitted beam. The noise requirement (1) is for interfering-beam misalignments up to  $300 \mu\text{rad}$ , a statement that comes from a top-level breakdown and was adopted as a conservative and rather stringent one [8, 9]. Since the telescope reduces the misalignment by the magnification, a  $300 \mu\text{rad}$  angle means that, in the sky, the noise requirement (1) is for reception angles  $\beta_0$  up to  $2.2 \mu\text{rad}$ .

To cope with a  $10 \text{ nrad}/\sqrt{\text{Hz}}$  jitter [3, 4], the jitter transfer function must be constrained to  $\langle \xi^2 \rangle_{z_n^m}^{1/2} \lesssim 1 \text{ pm/nrad}$ , as indicated by the dashed line in Fig. 8. By considering (31), where  $\alpha_0 = 0$  mrad and  $\beta_0 = 2 \mu\text{rad}$ , this means that the root-mean-square aberrations of the wavefronts must be constrained to 97 mrad (equivalently, to  $\lambda/65$ ). Furthermore, if we take the  $\langle \xi^2 \rangle_{z_n^m}^{1/2}$  dispersion (one standard deviation, see Fig. 8) into account, the the root-mean-square aberrations must be constrained to 70 mrad (equivalently, to  $\lambda/90$ ).

To investigate how the heterodyne phase depends on the specific set of Zernike amplitudes, we calculated the  $|\nabla_\alpha \phi_{\text{far}}|_0$  derivative for  $10^4$  random aberrations of the transmitted wavefront constrained by  $\sigma_S = 74$  mrad. After sorting the results in ascending  $|\nabla_\alpha \phi_{\text{far}}|_0$  order, Fig. 9 shows the  $|\nabla_\alpha \phi_{\text{far}}|_0$  moving-average and Fig. 10 shows the moving average of the Zernike amplitudes and correlation of the defocus and spherical aberrations. The same results hold for the phase sensitivity to the receiver jitter,  $|\nabla_\beta \phi_\Xi|_0$ .

Figure 9 shows that there is room for improvements by identifying how aberrations (having the same root-mean-square amplitude) combine constructively or destructively. Figure 10 (left) shows that a low sensitivity is correlated to small defocus and astigmatism. This is consistent with (27), because – on the average and with the  $w'_{\text{TX}} = 1$  choice made, see Fig. 11 – the leading  $g_2(w'_{\text{TX}})$  term of  $|\nabla_\alpha \phi_{\text{far}}|_0^2$  is dominated by the coefficients of the  $|z_2^0|^2$  and  $|z_2^2|^2$  amplitudes. Also, a low sensitivity correlates to aberrations having the largest spherical aberration because the coefficient of the  $|z_4^0|^2$  amplitude is the smallest. Figure 10 (right) shows that correlated defocus and spherical aberrations combine to keep sensitivity low. In fact, they contribute with opposite signs to (27).

## 6. Conclusion

Heterodyne interferometry, where laser beams are simultaneously transmitted and received by onboard telescopes, will sense the separation of the LISA spacecraft down to picometre sensitivity. Due to the interaction with the wavefront aberrations, telescope jitter affects the measured distances. In previous papers [10, 11], we developed surrogates of the far-field

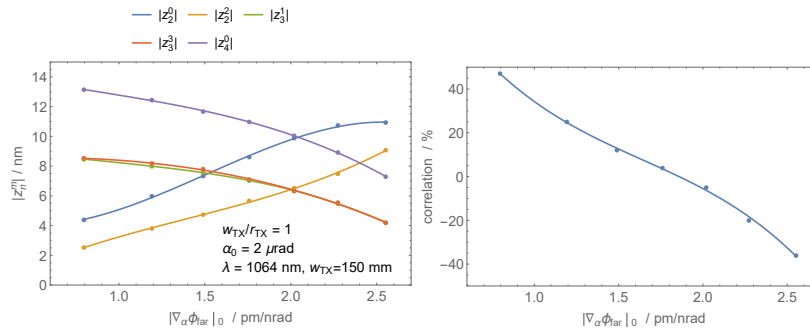


Fig. 10. First and second order statistics of the Zernike amplitudes of  $10^4$  random aberrations of the transmitted wavefront sorted according increasing sensitivity to the jitter. The aberrations are constrained by  $\sigma_S = 74 \text{ mrad}$ . Left: moving average of  $|z_n^m|$  over 2500 element windows, shifted by 1250 elements. Right: correlation of the defocus and spherical aberrations over 2500 element windows, shifted by 1250 elements.

and heterodyne-signal phases, in the form of polynomial expansions, that allow for reduced computational loads and analytic evaluation of the measurement noise.

We build on these separate investigations by using them to map analytically the spacecraft jitter into the phase noise of the heterodyne signal. Here, we combined the wavefront aberrations and jitters in a global computation, including far-field propagation, non-ideal reception, and heterodyne detection of the accumulated phase. Also, we averaged analytically the jitter transfer function over transmission and reception aberrations constrained by given root-mean-square amplitudes and developed criteria for trading off between allocations for aberrations, jitters, designs, and operations.

After fixing the root-mean-square aberrations, the jitter-induced noise depends on the radii of the transmitted and detected beams, the telescope and detector apertures, and the transmission and reception angles. To achieve the targeted performance, using the present estimates of the radii, apertures, angles, and jitter [3, 4], the root-mean-square aberrations must be less than  $97 \text{ mrad}$  (equivalently,  $\lambda/65$ ). This figure is significantly more demanding than the present estimate [3, 4].

Future calculations of the wavefront aberrations in the far field, the aberration impact on the interferometric signal, and the aberrations and jitter effect on the measurement of the spacecraft separation will require dedicated numerical tools. Our parametric surrogate is a test-bed to validate them.

## Appendix: Far-field and interference phases

In [10, 11], the coefficients  $a_{ij}$  and  $b_{ij}$  of the far-field and interference phases (18) and (21) have been calculated with the aid of Mathematica [13] by limiting the aberrations of the transmitted

and detected wavefronts to defocus, astigmatism, coma, trefoil, and spherical. Hence,

$$a_{00} = b_{00} = A_2 z_2^0 + A_4 z_4^0 + \text{II and III order terms}, \quad (36)$$

$$a_{10} = b_{10} = B \cos(\theta_3^3 - \theta_2^2) |z_3^3| |z_2^2| + C \cos(\theta_2^2 - \theta_3^1) |z_3^1| |z_2^2| \\ + D \cos(\theta_3^1) |z_3^1| |z_2^0| + G \cos(\theta_3^1) |z_3^1| |z_4^0|, \quad (37)$$

$$a_{01} = b_{01} = B \sin(\theta_3^3 - \theta_2^2) |z_3^3| |z_2^2| + C \sin(\theta_2^2 - \theta_3^1) |z_3^1| |z_2^2| \\ + D \sin(\theta_3^1) |z_3^1| |z_2^0| + G \sin(\theta_3^1) |z_3^1| |z_4^0|, \quad (38)$$

$$a_{20} = b_{20} = E z_2^0 + F \cos(\theta_2^2) |z_2^2| + H z_4^0, \quad (39)$$

$$a_{02} = b_{02} = E z_2^0 - F \cos(\theta_2^2) |z_2^2| + H z_4^0, \quad (40)$$

$$a_{11} = b_{11} = 2F \sin(\theta_2^2) |z_2^2|. \quad (41)$$

The  $A_2, A_4, B, C, D, E, F, G$ , and  $H$  coefficients

$$A_2 = \frac{1 + e^{2/w'^2}}{1 - e^{2/w'^2}} + w'^2, \quad (42)$$

$$A_4 = 1 + \frac{3(1 + e^{2/w'^2})w'^2}{1 - e^{2/w'^2}} + 3w'^2, \quad (43)$$

$$B = -\frac{2 + 3w'^2 + 3w'^4}{1 - e^{2/w'^2}} - \frac{3}{2}w'^6, \quad (44)$$

$$C = -\frac{2 + 5w'^2 + (7 + 2e^{2/w'^2})w'^4}{1 - e^{2/w'^2}} - \frac{9}{2}w'^6, \quad (45)$$

$$D = \frac{4e^{2/w'^2} + 12e^{2/w'^2}w'^2 - 2(2 + e^{2/w'^2})(1 - e^{2/w'^2})w'^4}{(1 - e^{2/w'^2})^2} - 6w'^2, \quad (46)$$

$$G = \frac{12e^{2/w'^2}w'^2 - 6(2 - 9e^{2/w'^2} + e^{4/w'^2})w'^4 - 6(7 - 2e^{2/w'^2} + 5e^{4/w'^2})w'^6}{(1 - e^{2/w'^2})^2} \\ - 45w'^8, \quad (47)$$

$$E = \frac{2e^{2/w'^2}}{(1 - e^{2/w'^2})^2} - \frac{1}{2}w'^4, \quad (48)$$

$$F = -\frac{1 + w'^2}{1 - e^{2/w'^2}} - \frac{1}{2}w'^4, \quad (49)$$

$$H = \frac{6e^{2/w'^2}w'^2 - 3(1 - e^{4/w'^2})w'^4/2}{(1 - e^{2/w'^2})^2} - w'^6, \quad (50)$$

depend on the normalized radius  $w'$  (see Fig. 11) where, in (18) ( $a_{ij}$  coefficients),

$$w' = \sqrt{2}w_{\text{TX}}/r_{\text{TX}} \quad (51)$$

and, in (21) ( $b_{ij}$  coefficients),

$$w' = w_{\text{RX}}/r_D = w_{\text{TX}}/r_{\text{RX}}. \quad (52)$$

Here,  $w_{\text{TX}}$  is the  $1/e^2$  radius of the transmitted beam and  $w_{\text{RX}}$  is the harmonic mean of the  $1/e^2$  radii of the interfering beams.

## Funding

European Space Agency (1550005721, Metrology Telescope Design for a Gravitational Wave Observatory Mission).



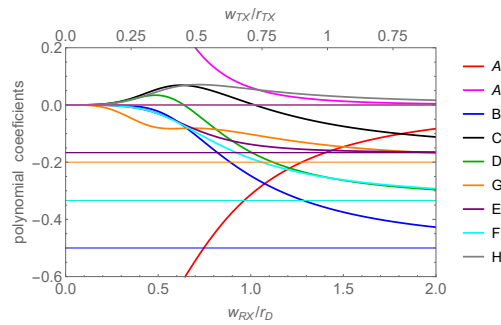


Fig. 11. Coefficients of the (36-B6) polynomials. The horizontal lines are asymptotic values (plane-wave approximation). The limits of  $A_2$  and  $A_4$  when  $w_{\square}/r_{\square} \rightarrow 0$  are  $\pm 1$ .

## Disclosures

The authors declare that there are no conflicts of interest related to this article.

## References

1. K. Danzmann and A. R. diger, "LISA technology concept, status, prospects," *Class. Quantum Gravity* **20**, S1–S9 (2003).
2. O. Jennrich, "LISA technology and instrumentation," *Class. Quantum Gravity* **26**, 153001 (2009).
3. K. Danzmann, "LISA Laser Interferometer Space Antenna – A proposal in response to the ESA call for L3 mission concepts," Tech. Rep. LISA\_L3\_20170120, Lisa Consortium (2017).
4. LISA Instrument Group, "LISA Payload Description Document," Tech. Rep. ESA-L3-EST-INST-DD-001, ESA (2017).
5. M. Armano, H. Audley, G. Auger, J. T. Baird, M. Bassan, P. Binetruy, M. Born, D. Bortoluzzi, N. Brandt, M. Caleno, L. Carbone, A. Cavalleri, A. Cesarini, G. Ciani, G. Congedo, A. M. Cruise, K. Danzmann, M. de Deus Silva, R. De Rosa, M. Diaz-Aguiló, L. Di Fiore, I. Diepholz, G. Dixon, R. Dolesi, N. Dunbar, L. Ferraioli, V. Ferroni, W. Fichter, E. D. Fitzsimons, R. Flatscher, M. Freschi, A. F. García Marín, C. García Marirrodrga, R. Gerndt, L. Gesa, F. Gibert, D. Giardini, R. Giusteri, F. Guzmán, A. Grado, C. Grimaldi, A. Grynagier, J. Grzysch, I. Harrison, G. Heinzel, M. Hewitson, D. Hollington, D. Hoyland, M. Hueller, H. Inchauspé, O. Jennrich, P. Jetzer, U. Johann, B. Johlander, N. Karnesis, B. Kaune, N. Korsakova, C. J. Killow, J. A. Lobo, I. Lloro, L. Liu, J. P. López-Zaragoza, R. Maarschalkerweerd, D. Mance, V. Martín, L. Martin-Polo, J. Martino, F. Martin-Porqueras, S. Madden, I. Mateos, P. W. McNamara, J. Mendes, L. Mendes, A. Monsky, D. Nicolodi, M. Nofrarias, S. Paczkowski, M. Perreux-Lloyd, A. Petiteau, P. Pivato, E. Plagnol, P. Prat, U. Ragnit, B. Raïs, J. Ramos-Castro, J. Reiche, D. I. Robertson, H. Rozemeijer, F. Rivas, G. Russano, J. Sanjuán, P. Sarra, A. Schleicher, D. Shaul, J. Slutsky, C. F. Sopuerta, R. Stanga, F. Steier, T. Sumner, D. Texier, J. I. Thorpe, C. Trenkel, M. Tröbs, H. B. Tu, D. Vetrugno, S. Vitale, V. Wand, G. Wanner, H. Ward, C. Warren, P. J. Wass, D. Wealthy, W. J. Weber, L. Wissel, A. Wittchen, A. Zambotti, C. Zanon, T. Ziegler, and P. Zweifel, "Sub-femto-g free fall for space-based gravitational wave observatories: Lisa pathfinder results," *Phys. Rev. Lett.* **116**, 231101 (2016).
6. D. I. Robertson, P. McNamara, H. Ward, and J. Hough, "Optics for lisa," *Class. Quantum Gravity* **14**, 1575 (1997).
7. P. L. Bender, "Wavefront distortion and beam pointing for LISA," *Class. Quantum Gravity* **22**, S339 (2005).
8. M. Chwalla, K. Danzmann, G. F. Barranco, E. Fitzsimons, O. Gerberding, G. Heinzel, C. J. Killow, M. Lieser, M. Perreux-Lloyd, D. I. Robertson, S. Schuster, T. S. Schwarze, M. Tröbs, H. Ward, and M. Zwetz, "Design and construction of an optical test bed for LISA imaging systems and tilt-to-length coupling," *Class. Quantum Gravity* **33**, 245015 (2016).
9. M. Troebs, S. Schuster, M. Lieser, M. Zwetz, M. Chwalla, K. Danzmann, G. F. Barranco, E. D. Fitzsimons, O. Gerberding, G. Heinzel, C. J. Killow, M. Perreux-Lloyd, D. I. Robertson, T. S. Schwarze, G. Wanner, and H. Ward, "Reducing tilt-to-length coupling for the LISA test mass interferometer," *Class. Quantum Gravity* **35**, 105001 (2018).
10. C. P. Sasso, G. Mana, and S. Mottini, "Coupling of wavefront errors and jitter in the LISA interferometer: far-field propagation," *Class. Quantum Gravity* **35**, 185013 (2018).
11. C. P. Sasso, G. Mana, and S. Mottini, "Coupling of wavefront errors and pointing jitter in the LISA interferometer: misalignments of the interfering wavefronts," *Class. Quantum Gravity* **35**, 245002 (2018).
12. J. A. Rice, *Mathematical Statistics and Data Analysis* (Duxbury Press, 2006).
13. Wolfram Research, Inc., "Mathematica, Version 11.2," (2017). Champaign, IL.
14. G. B. Folland, "How to integrate a polynomial over a sphere," *The Am. Math. Mon.* **108**, 446–448 (2001).
15. D. E. Knuth, *The Art of Computer Programming, Volume 2 (3rd Ed.): Seminumerical Algorithms* (Addison-Wesley Longman Publishing Co., Inc., Boston, MA, USA, 1997).

16. M. E. Muller, "A note on a method for generating points uniformly on  $N$ -dimensional spheres." Commun. ACM **2**, 19–20 (1959).